Responsive nanoplatform for persistent luminescence "turn-on" imaging and "on-demand" synergistic therapy of bacterial infection

Bei-Bei Wang [a,b,c,1], Li-Xia Yan [a,b,c,1], Li-Jian Chen [a,b,c], Xu Zhao [a,b,c], Xiu-Ping Yan [a,b,c,d,*]

[a] State Key Laboratory of Food Science and Technology, Jiangnan University, Wuxi 214122, China
[b] International Joint Laboratory on Food Safety, Jiangnan University, Wuxi 214122, China
[c] Institute of Analytical Food Safety, School of Food Science and Technology, Jiangnan University, Wuxi 214122, China
[d] Key Laboratory of Synthetic and Biological Colloids, Ministry of Education, Jiangnan University, Wuxi 214122, China

GRAPHICAL ABSTRACT
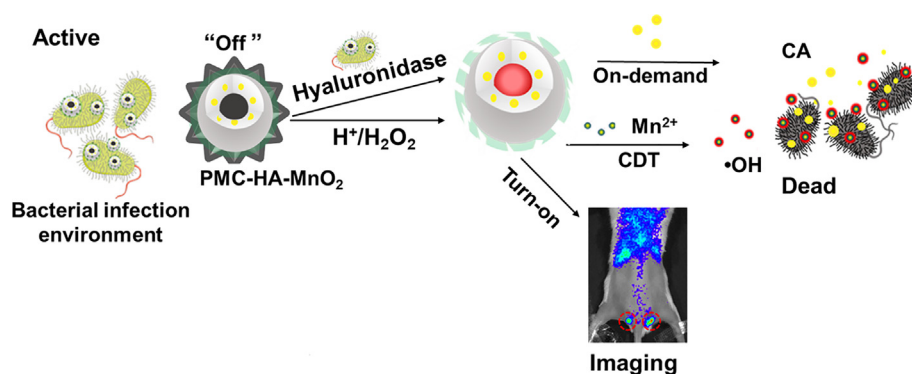
ABSTRACT

Multifunctional nanotheranostic platforms are emerging for the treatment of bacterial infections. Uncontrollable drug release and poor response in target location leads to inefficient therapy and failure to offer timely antibacterial monitoring. Here, we report a multifunctional nanoplatform that can be triggered by the bacterial microenvironment for effective bacterial killing and high-sensitive persistent luminescence (PL) "turn-on" imaging. Hyaluronic acid (HA) is grafted on the surface of mesoporous silica-coated persistent luminescence nanoparticles (PLNPs@MSN) loaded with cinnamaldehyde (CA). Further in situ growth of MnO_2 shells gives PLNPs@MSN@CA-HA-MnO_2 (PMC-HA-MnO_2). MnO_2 shell of PMC-HA-MnO_2 can be reduced to Mn^{2+} by the H_2O_2 in the bacterial microenvironment to trigger persistent luminescence (PL) "turn-on" imaging along with chemodynamic therapy (CDT). Meanwhile, HA can response to bacterially secreted hyaluronidase to make the packaged CA release controllable and "on-demand". Consequently, PMC-HA-MnO_2 enables effective response to bacterial-infected region, ensuring high-sensitive "turn-on" imaging, synergistic CDT, accurate targeting and "on-demand" CA release to give great antibacterial effect. This nanoplatform has great potential for the diagnosis and treatment of multidrug-resistant bacterial infection with high specificity and efficiency.

© 2021 Elsevier Inc. All rights reserved.

⁎ Corresponding author.
    E-mail address: xpyan@jiangnan.edu.cn (X.-P. Yan).
 [1] These authors contributed equally to this paper.

1. Introduction

Pathogenic bacterial infection, especially complex infections caused by antibiotic-resistant bacteria has aroused increasing concerns due to the great harm to human health [1,2]. Currently, the most widely accepted treatment for bacterial infection is antibiotics. However, the overuse of antibiotics leads to an increase in bacterial resistance. For example, methicillin-resistant *Staphylococcus aureus* (MRSA), the main cause of skin and soft tissue intractable infection, is produced due to inappropriate antibiotic treatment. MRSA can weaken the therapeutic effect of antibiotics, and causes a high mortality [3–7]. It is regrettable that the development of new antibiotics has been restricted over the past decades, while new multidrug-resistant (MDR) bacteria are emerging at a much faster rate than new antibiotics [8,9]. Therefore, it is in urgent to develop alternative therapeutic strategies or effective antimicrobial agents with low drug resistance for MDR bacteria treatment.

Phytochemicals, extracted from plants, emerge as effective alternatives to conventional synthetic antibiotics for addressing the shortages of antibiotics. Essential oils (EOs), as "green" bactericides, are well known to exhibit excellent biocompatibility, biological and broad spectra antimicrobial activity [10]. Compared with traditional synthetic antibiotics, the antimicrobial mechanism of EOs is complex, and thus bacteria are not easy to develop drug resistance. EOs are safe and non-toxic to vertebrates within the range of antibacterial concentration and can be easily biodegraded and metabolized. Importantly, EOs have a wide range of sources and are easily acquired, providing a large inventory for new antibacterial agents [11–14]. However, EOs also have their own shortcomings in bacteriostasis, such as poor solubility in aqueous solution and non-selectivity for infection, which decreases the therapeutic effect and seriously hinders their widespread application [15,16]. Therefore, it is still a challenge to establish an effective delivery system to ensure the most effective use of EOs. Nanoparticle-based drug delivery systems are expected to be one of the methods to solve this problem and give full play to the antibacterial effect of EOs.

Manganese is one of the most commonly metal elements in disease treatment for its good biosafety and rich quantity of valence states [17–19]. Manganese dioxide (MnO_2) is highly favored for its catalase-like ability as it can convert endogenous detrimental peroxide (H_2O_2) into salutary oxygen (O_2), and the released manganese ions (Mn^{2+}) can achieve chemodynamic therapy (CDT) by exerting Fenton-like activity to generate •OH from H_2O_2 in weak acidic environment [20–25]. Such Mn^{2+}-mediated CDT further extends the potential of Mn^{2+} as a nanotheranostic agent. MnO_2 is also a good light quenching agent with wide absorption from ultraviolet to visible region. Therefore, MnO_2 is a good candidate to serve as fluorescence nano-quencher, nanotheranostic agent and H_2O_2 recognizer in weak acidic environment.

Nowadays, intelligent nanoprobes enabling imaging and "on-demand" drug delivery have received great attention owing to the excellent ability to visualize lesions and accurately target to the site of bacterial infection with low side effects. In recent years, optical materials like lanthanide fluorescent nanoparticles and quantum dots have been used for diagnosis and therapy [26–29]. But, conventional fluorescent nanoprobes require in situ excitation which often causes tissue damage. Especially, "always on" imaging leads to background interference to the targeted position, making it difficult to accurately determine the targeted position in the early stage. Near-infrared (NIR)-emitting persistent luminescence nanoparticles (PLNPs) are promising optical materials in biomedical imaging and long-term *in vivo* tracing due to the merits of deep tissue penetration without in situ excitation and repetitive activation with red LED light [30–32].

Here, we show the design and preparation of a bacterial microenvironment-responsive and hyaluronidase-activated "on-demand" delivery antibacterial nanoplatform for *in vivo* persistent luminescence (PL) "turn-on" imaging and drug-CDT synergistic therapy of bacterial infection. In this nanoplatform, cinnamaldehyde (CA) with broad bactericidal ability is used as an alternative to antibiotics [33]. Mesoporous silica (MSN)-coated PLNPs (PLNPs@MSN) with long PL and plenty of pores serves as ideal visualized nanocarrier for CA [34]. Hyaluronic acid (HA), which can be hydrolyzed by the overexpressed hyaluronidase (Hyal) produced by bacteria at the infection site [35–37], is used as a capping agent for CA and the "on-demand" releasing gatekeeper. HA is grafted to the surface of PLNPs@MSN loaded with CA to obtain PLNPs@MSN@CA-HA (PMC-HA). MnO_2 shells are grown on PMC-HA to serve as fluorescence nano-quencher, nanotheranostic agent and H_2O_2 recognizer in weak acidic environment. Thus, a bacterial microenvironment-responsive nanoplatform (PMC-HA-MnO_2) is developed. The MnO_2 shell and HA capping are the two switches which can be opened specifically by highly expressed H_2O_2 and Hyal in the bacterial infection microenvironment, ensuring "turn-on" PL imaging, "on-demand" release of CA and full utilization of CDT. The as-prepared multifunctional nanoplatform exhibits great potential for visualized treatment of MDR bacterial infection.

2. Experimental section

2.1. Synthesis of PLNPs@MSN-NH$_2$

NIR-emitting $Zn_{1.2}Ga_{1.6}Ge_{0.2}O_4$:$Cr^{3+}$ PLNPs was synthesized by a hydrothermal method combined with further calcination [38]. PLNPs@MSN was prepared according to Zhang et al [32] with minor modification (Supporting Information). PLNPs@MSN were further aminated as follows. The obtained PLNPs@MSN (100 mg) were dispersed in NaOH solution (5 mmol L^{-1}, 100 mL) and vigorously stirred overnight to obtain hydroxyl-PLNPs@MSN (PLNPs@MSN-OH). Then, PLNPs@MSN-OH (100 mg) was dispersed in ethanol (100 mL) with sonication and 3-amino propyl triethoxysilane (APTES) (400 μL) was dropwise added under vigorous stirring. The reaction mixture was incubated at 60 °C for 12 h. The resulting PLNPs@MSN-NH$_2$ was collected via centrifugation, washed with ethanol and dried under vacuum.

2.2. CA loading and HA capping of PLNPs@MSN

PLNPs@MSN-NH$_2$ (20 mg) and CA (20 mg) were dispersed in ethanol (10 mL) for 24 h stirring. The CA-loaded nanoparticles PLNPs@MSN@CA was separated via centrifugation for further HA capping. HA (30 mg) was dissolved in a small amount of water firstly and then activated by NHS (120 mg) and EDC (60 mg) in PBS (pH 6.0, 30 mL). The solution pH was adjusted to 8.0 with NaOH solution (1 mol L^{-1}) after surface activation for 1 h. Then, the obtained PLNPs@MSN@CA was added. After reaction for 12 h, the resulting PLNPs@MSN@CA-HA (PMC-HA) was collected by centrifugation and washed with ultrapure water to remove the untreated HA.

2.3. Preparation of PLNP@MSN@CA-HA-MnO$_2$ (PMC-HA-MnO$_2$)

Poly allylamine hydrochloride (15 kDa, 37.5 mg mL^{-1}) was added into the PMC-HA solution (1 mg mL^{-1} as PLNPs@MSN). After stirring for 4 h, the nanoparticles were acquired by centrifugation and then redisperse in pure water. Then, $KMnO_4$ aqueous solutions (5 mmol L^{-1}, 300 μL) added dropwise into the above suspension

under magnetic stirring until the solution turned brown. The final PMC-HA-MnO$_2$ nanoparticles were centrifuged at 8000 rpm for 10 min and washed with pure water for three times. The obtained PMC-HA-MnO$_2$ nanoparticles were then dispersed in PBS (pH 5.5, 10 mmol L^{-1}) and were stored at 4 °C for further use.

2.4. Bacterial culture and antibacterial experiments

S. aureus, *E. coli* and MRSA were incubated in 5 mL Luria Bertani broth medium with shaking (200 rpm) at 37 °C for 12 h. 1 mL bacteria solution ($\sim$10^9 CFU mL^{-1}) was mixed with PMC-HA-MnO$_2$ solution (30, 60, 100, 200, 300, 400, 500 µg mL^{-1}, as PLNPs@MSN) in the presence of 0.2 mmol L^{-1} H$_2$O$_2$ at pH 5.5 for 12 h. The turbidity of bacteria suspensions (OD, 600 nm) was recorded on a multifunctional microplate reader.

To further prove the bactericidal effect of PMC-HA-MnO$_2$, bacteria solution ($\sim$10^9 CFU mL^{-1}) was incubated with six groups (PBS, PBS + H$_2$O$_2$, PLNPs@MSN-MnO$_2$, PLNPs@MSN-MnO$_2$ + H$_2$O$_2$, PMC-HA, PMC-HA-MnO$_2$ + H$_2$O$_2$; PLNPs@MSN-MnO$_2$, PMC-HA and PMC-HA-MnO$_2$, 300 µg mL^{-1} as PLNPs@MSN; pH 5.5; H$_2$O$_2$, 0.2 mmol L^{-1}) for 12 h. After incubation, the turbidity of bacteria suspensions (OD, 600 nm) was recorded on a multifunctional microplate reader.

The conventional plate counting method was adopted to assess the colonies after the treatment of the above six groups visually. Bacteria suspensions (100 µL) from the above six groups after incubation were smeared into LB agar plate and cultivated at 37 °C for 24 h.

2.5. Murine infection model

Female Balb/c mice (4–5 weeks) were purchased from Changzhou Cavens Laboratory Animal Co. Ltd (Changzhou, China). The mice were fed with a standard laboratory diet and water. All experiments were conformed to the Jiangnan University of Use and Care of Laboratory Animals, and performed ethically and humanely. The MRSA-infected mouse model was built to evaluate PL "turn-on" imaging and antibacterial effect of PMC-HA-MnO$_2$ *in vivo*. The subcutaneous abscesses models were established by a subcutaneous injection of MRSA PBS buffer (150 µL, about 10^8 CFU mL^{-1}) at the back of each mouse after anesthetization.

2.6. In vivo PL "turn-on" imaging of MRSA-infected subcutaneous abscesses

The anesthetized subcutaneous abscess mice were treated with PLNPs@MSN, PMC-HA and PMC-HA-MnO$_2$ (200 µL, 2 mg mL^{-1} as PLNPs@MSN) by intravenous injection, respectively. The PL distribution of the implanted PMC-HA-MnO$_2$ were collected on IVIS spectrum imaging system at the specified time points (5 min, 4 h, 6 h, 12 h, day 2, day 4, day 6, day 8 and day 10) under bioluminescence mode with an open filter (60 s of acquisition). The PL distribution of PLNPs@MSN and PMC-HA were monitored for comparison. The PLNPs@MSN, PMC-HA and PMC-HA-MnO$_2$ were irradiated by a 254 nm UV lamp for 5 min before injection. The re-excited imaging was obtained by irradiating mice with 650 nm LED light (5000 lm) for 2 min before collecting signals.

2.7. In vivo antibacterial therapy

After 24 h MRSA infection, the mice were treated with antibacterial therapy. The infected mice (n = 15) were randomly divided into three groups (five mice for each group): (I) PBS, (II) PMC-HA, (III) PMC-HA-MnO$_2$. The healthy mice without any treatment (n = 5) were set as the control group. PMC-HA and PMC-HA-MnO$_2$ (200 µL, 2 mg mL^{-1} as PLNPs@MSN) were intravenously

injected into the mice of group II and group III. The body weight of mice was measured every day. For histological analysis, all mice were sacrificed after treatment for 10 days. The wound skin tissues and major organs (heart, liver, lung, kidney, and spleen) were harvested for H&E staining.

3. Results and discussion

3.1. Design and characterization of the PMC-HA-MnO$_2$

Scheme 1A illustrates the design and fabrication of the multifunctional nanoplatform PMC-HA-MnO$_2$. Zn$_{1.2}$Ga$_{1.6}$Ge$_{0.2}$O$_4$:Cr^{3+} PLNPs was prepared as the core because of its long afterglow lifetime and reactivatable NIR-persistent luminescence [39]. MSN was coated on the surface of PLNPs to load and carry CA. PMC-HA was prepared by capping HA on the surface of PLNPs@MSN@CA via amide reaction to avoid CA leaking during treatment and to ensure effective treatment without harm to normal cells. Afterwards, KMnO$_4$ was in situ reduced to form MnO$_2$ shell on the surface of PMC-HA in the presence of cationic polyelectrolyte poly allylamine hydrochloride [40,41]. Here, MnO$_2$ not only acts as the fluorescence nano-quencher, but also the nanotheranostic agent and H$_2$O$_2$ recognizer in weak acidic environment. As such, the multifunctional nanoplatform PMC-HA-MnO$_2$ with no PL was prepared.

Scheme 1B shows the multifunctional nanoplatform PMC-HA-MnO$_2$ for bacterial microenvironment-responsive "turn-on" imaging and hyaluronidase-activated "on-demand" CA release combined with CDT. PMC-HA-MnO$_2$ would be accumulated in the acidic bacterial infection abscesses due to the protonation of the amino group. The MnO$_2$ shell is broken up because of the acidic environment and the overproduction H$_2$O$_2$ in the bacteria infection microenvironment [42,43]. As a result, the PL of PLNPs is turned on, and the produced Mn^{2+} serves as a Fenton-like initiator for CDT. Meanwhile, HA is decomposed by Hyal secreting from bacteria, and the encapsulated CA is released on demand to directly kill bacteria. The infected site is illuminated by the restored PL to monitor the process of treatment. Thus, the multifunctional nanoplatform not only enables the bacteria microenvironment triggered PL "turn-on" imaging, but also drug-CDT synergistic therapy of bacteria.

The as-prepared PLNPs was well dispersed with the mean particle diameter of 16.2 ± 2.5 nm (based on 100 randomly selected nanoparticles) (Fig. 1A and B), and the crystal lattice characteristic peaks of ZnGa$_2$O$_4$ (JCPDS 38-1240) and Zn$_2$GeO$_4$ (JCPDS 25-1018) (Fig. 1C). The PLNPs in aqueous solution exhibited a NIR luminescence peak at 698 nm (Fig. S1A). The PLNPs gave the quantum yield of 33.4%, and showed good long PL performance (Fig. S1B). The PL signal attenuated quickly in a short period, then gradually levelled off and became stable for a long time. In addition, the PLNPs could be repeatedly excited by a red LED lamp to recover PL, allowing long-term autofluorescence-free bioimaging *in vivo*. The modification of MSN and HA made only a slight decline of the PL of PLNPs@MSN and PMC-HA, respectively. In contrast, the coating of MnO$_2$ shell had the PL of PMC-HA-MnO$_2$ almost completely quenched (Fig. S1C). Thus, the PL of PMC-HA-MnO$_2$ remained "off" in normal physiological environments. MnO$_2$ shell could be decomposed by H$_2$O$_2$ in the acidic environment, but acidic environment or H$_2$O$_2$ alone could not break down MnO$_2$ (Fig. S1D). This property made PMC-HA-MnO$_2$ selective to bacterial infection microenvironment.

The as-prepared PLNPs@MSN exhibited mesoporous core–shell structure with an average diameter of 100 ± 2.1 nm (Fig. 1D), showed the characteristic peaks of PLNPs along with a new wide peak near 23° for MSN (Fig. 1E). The coated MSN also had the characteristic peak near 3.18° in low angle XRD pattern, further proving
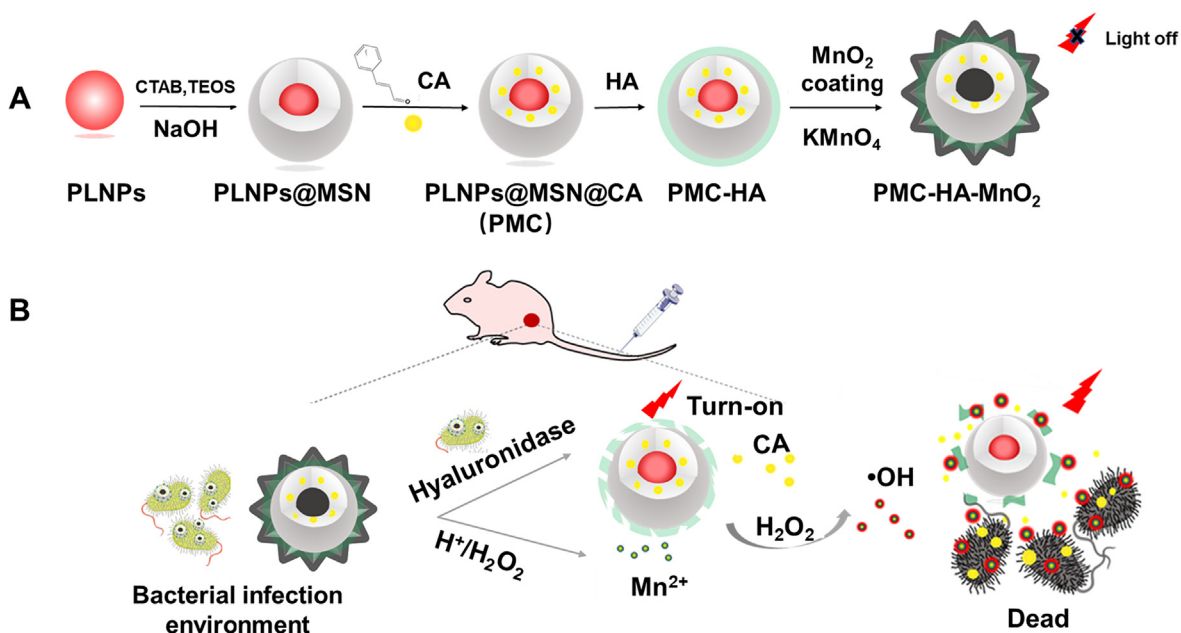
Scheme 1. (A) Illustration for the preparation of PMC-HA-MnO$_2$. (B) Schematic of PMC-HA-MnO$_2$ for bacterial microenvironment-responsive PL "turn-on" imaging and hyaluronidase-activated "on-demand" CA release combined with CDT.

a well-ordered porous structure similar to MCM-41 of the hexagonal arrangements (Fig. 1F, Inset). Besides, the PLNPs@MSN offered the surface area (291 m^2 g^{-1}) and the pore volume (0.665 cc g^{-1}) with a well-defined pore size (3.2 nm) (Fig. 1F), which provided abundant sites for efficient CA loading.

PMC-HA-MnO$_2$ particles were still about 100 nm in dimeter with well-defined spherical morphology and coarse surface (Fig. 1G). After the decomposition of MnO$_2$ on PMC-HA-MnO$_2$, the PMC-HA particles regained a smooth surface (Fig. 1G, Inset). Most of Zn, Ga and Ge were in the core while Si and O in the whole nanostructures, indicating the coating of MSN. The element Mn was mainly in the outer layer, indicating the successful preparation of MnO$_2$ shell (Fig. S2). X-ray photoelectron spectroscopy (XPS) spectra (Fig. 1H) and the absorption spectra (Fig. S3A) proved the successful preparation of PMC-HA-MnO$_2$. Two peaks at 653.2 eV and 641.6 eV in XPS high-resolution scans spectrum accorded with the Mn(IV)2p$_{1/2}$ and Mn(IV)2p$_{3/2}$ spin orbit peaks of MnO$_2$ (Fig. 1I), further verifying the conversion of KMnO$_4$ into MnO$_2$. Two distinct peaks at 380 nm and 285 nm in the absorption spectra of PMC-HA-MnO$_2$ proved the MnO$_2$ coating and CA loading, respectively (Fig. S3B) [44]. The loading efficiency of CA was determined to be 33.1% by UV–vis spectroscopy (Fig. S4).

PMC-HA-MnO$_2$ gave no PL because of the quenching effect of MnO$_2$ shell (Fig. 1J). It exhibited a weak negative charge (-6.4 mV) at pH 7.4 and a positive charge (+12.3 mV) at pH 5.5 (Fig. 1K). Thus, PMC-HA-MnO$_2$ could bind to negatively charged bacteria cell wall at the site of acidic bacterial-infection abscesses. The hydrodynamic diameter increased from 106 nm for PLNPs to 396 nm for PMC-HA-MnO$_2$ because of the introduction of HA and MnO$_2$ (Fig. S1E). Time-dependent analysis of the PL emission spectra shows that PMC-HA was relatively stable at pH 5.5 or in the presence of 0.2 mmol L^{-1} H$_2$O$_2$ for 120 h (Fig. S1F). The Fourier transform infrared (FTIR) spectroscopic peaks around 1,407 and 1,637 cm^{-1} in PMC-HA and PMC-HA-MnO$_2$ (Fig. 1L) were attributed to the stretching vibration of C—N and amide C=O groups, respectively, showing the successful conjugation of HA [45].

3.2. H$_2$O$_2$-responsive property of PMC-HA-MnO$_2$

The responsivity of the developed PMC-HA-MnO$_2$ to H$_2$O$_2$ was demonstrated by the addition of different concentrations of H$_2$O$_2$ into PMC-HA-MnO$_2$ solution in pH 5.5. PMC-HA-MnO$_2$ itself showed no PL as a result of MnO$_2$ quenching effect (Fig. 2A). However, the presence of H$_2$O$_2$ made the PL of the PMC-HA-MnO$_2$ recovered (Fig. 2B) and the absorption characteristic peak of MnO$_2$ decrease (Fig. 2C), suggesting the decomposition of the MnO$_2$ shell because of the reduction of MnO$_2$ shell by H$_2$O$_2$. The influence of reaction time on the PL recovery of PMC-HA-MnO$_2$ was studied with 0.2 mmol L^{-1} H$_2$O$_2$ at pH 5.5 (Fig. 2D). The PL intensity increased quickly with reaction time and reached a plateau after 12 min. The restored PL of PMC-HA-MnO$_2$ with different concentrations of H$_2$O$_2$ was recorded on the IVIS imaging system (Fig. S5A). The NIR PL of PMC-HA-MnO$_2$ treated by H$_2$O$_2$ could be reactivated under red LED light excitation with little loss (Fig. S5B). The above results show that PMC-HA-MnO$_2$ could be triggered quickly by H$_2$O$_2$ in acid environment to realize the PL "turn-on" imaging.

3.3. Hyal-activated release

The responsive performance of PMC-HA-MnO$_2$ for CA release was investigated *in vitro* with Hyal as a stimulator. CA release from PMC-HA-MnO$_2$ was monitored up to 24 h. The released CA reached the maximum (approximately 42%) in acetate buffer containing Hyal (pH 5.0), but only about 10% in PBS (pH 7.4), acetate buffer without Hyal or with deactivated Hyal (Fig. 3A). In contrast, the released CA from the PMC-HA-MnO$_2$ incubated with the three kinds of bacteria in acetate buffer was 33.3% for *Staphylococcus aureus* (*S. aureus*), 24.9% for *Escherichia coli* (*E. coli*) and 25.6% for MRSA (Fig. S6). These results demonstrate that CA release from the PMC-HA-MnO$_2$ can be triggered by the artificially added Hyal or bacterially secreted Hyal. Furthermore, we evaluated the trigger behavior for CA release. As expected, CA release from PMC-HA-MnO$_2$ increased dramatically once Hyal was added to the system after 3 h (Fig. 3B), indicating that CA release was an enzyme stimuli-responsive process. The above results demonstrate that PMC-HA-
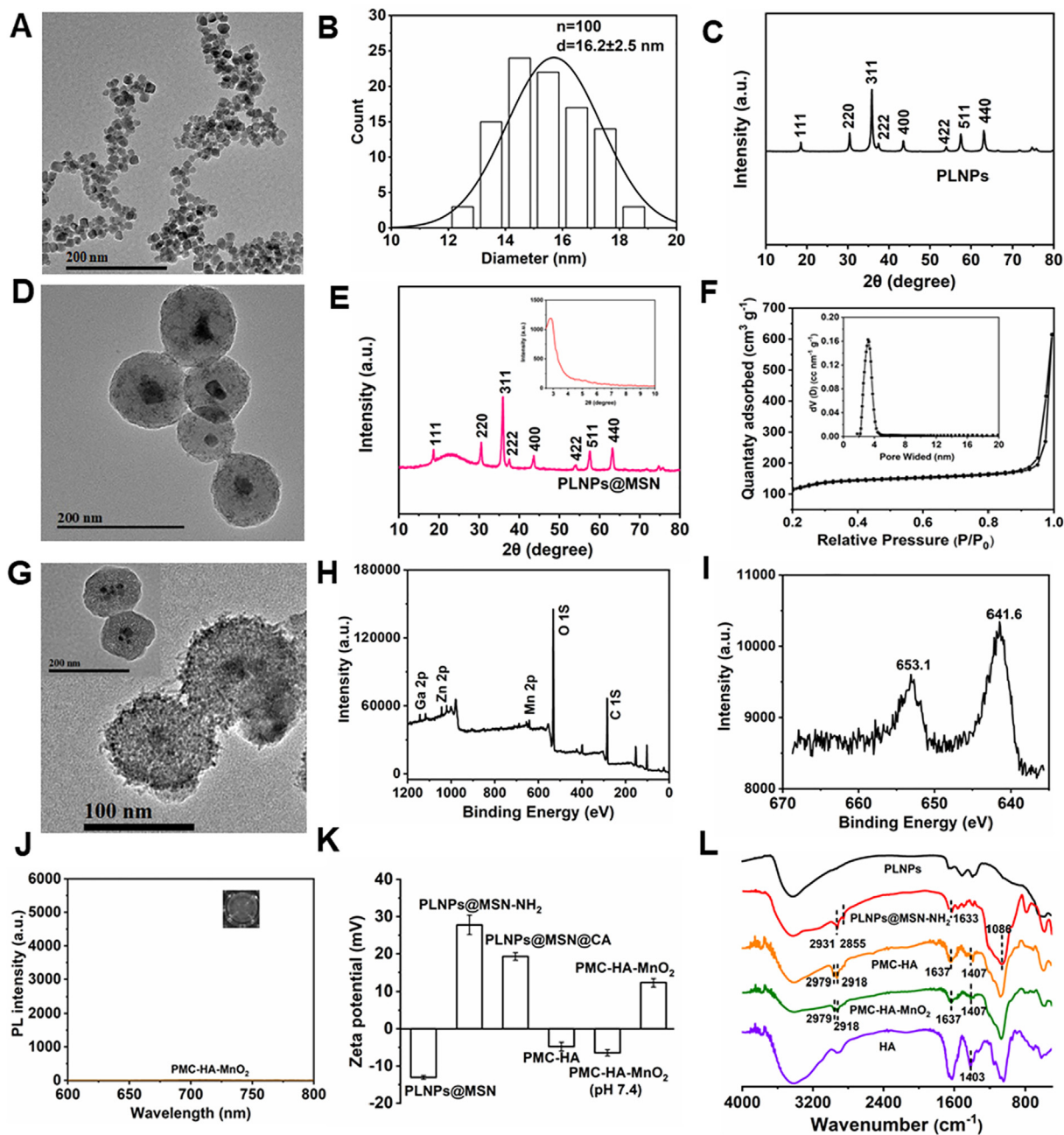
Fig. 1. Characterization of PLNPs: (A) TEM image. (B) Size distribution. (C) XRD spectrum. Characterization of PLNPs@MSN: (D) TEM image. (E) XRD spectrum (Inset: small-angle XRD spectrum). (F) Nitrogen adsorption–desorption isotherms (Inset: Pore size distribution of PLNPs@MSN). Characterization of PMC-HA-MnO$_2$: (G) TEM image (Inset: TEM image of PMC-HA). (H) XPS spectrum. (I) High-resolution Mn 2p spectrum. (J) PL spectrum of PMC-HA-MnO$_2$ aqueous solution (1 mg mL^{-1}, Inset: The image under UV excitation). (K) Zeta potential of PLNPs@MSN, PLNPs@MSN-NH$_2$, PLNPs@MSN@CA, PMC-HA and PMC-HA-MnO$_2$ (1 mmol L^{-1} PBS, pH 5.5). (L) FT-IR spectra of PLNPs, PLNPs@MSN-NH$_2$, PMC-HA, PMC-HA-MnO$_2$ and HA.

MnO$_2$ could act as an "on-demand" nanoplatform for treating bacterial infection.

3.4. Mn^{2+}- or PMC-HA-MnO$_2$-mediated Fenton-like reaction

Mn^{2+}-induced Fenton-like reaction was shown to realize CDT through •OH generation like Fe^{2+} [23]. Methylene blue (MB) with the ability of degradation of •OH, was chosen as an indicator for •OH generation. MnCl$_2$ was utilized as the source of Mn^{2+} for Fenton-like reaction. Fig. 4A shows a significant decrease in the absorbance of MB when it incubated with H$_2$O$_2$ and Mn^{2+} for 30 min, but no obvious variation in the absorbance of MB was observed with H$_2$O$_2$ or Mn^{2+} only. Fig. 4B shows that the absorbance of MB remained no change after incubating with PMC-HA, while the absorbance of MB gradually decreased with the increase in the concentration of PMC-HA-MnO$_2$ owing to the •OH generated by Mn^{2+} from MnO$_2$ shell. The result indicates that PMC-HA-MnO$_2$ possessed the ability for CDT through Mn^{2+}-induced Fenton-like reaction.

3.5. In vitro antimicrobial activity of PMC-HA-MnO$_2$

S. aureus, MRSA and *E. coli* were used as model bacteria to investigate the performance of PMC-HA-MnO$_2$ for *in vitro* antibacterial
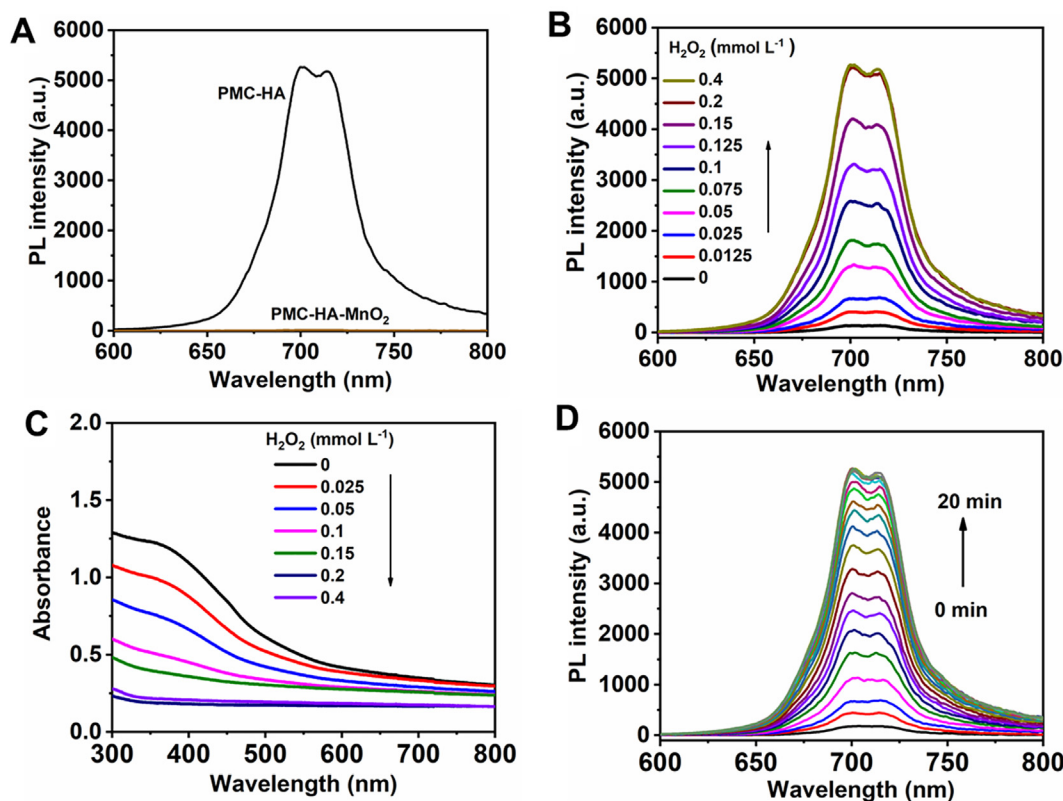
Fig. 2. (A) Quenching effect of MnO$_2$ shell on the PL intensity of PMC-HA (400 μg mL^{-1}). (B) PL emission spectra of PMC-HA-MnO$_2$ (400 μg mL^{-1}) treated with H$_2$O$_2$ at various concentrations with a reaction time of 15 min. (C) Absorption spectra of PMC-HA-MnO$_2$ (400 μg mL^{-1}) treated with H$_2$O$_2$ at various concentrations with a reaction time of 15 min. (D) Effect of reaction time on the PL emission spectra of PMC-HA-MnO$_2$ treated by H$_2$O$_2$ (PMC-HA-MnO$_2$, 400 μg mL^{-1}; H$_2$O$_2$, 0.2 mmol L^{-1}).
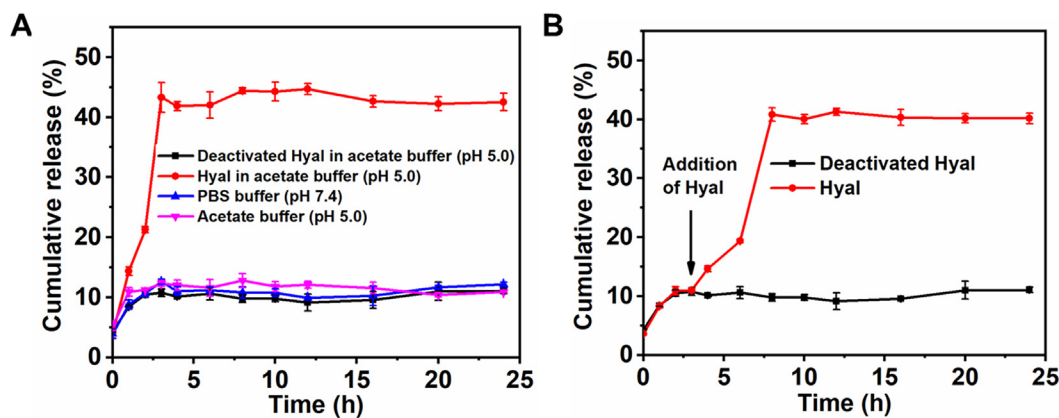

Fig. 3. (A) Release profiles of CA from PMC-HA-MnO$_2$ (1 mg mL^{-1}) in PBS only or with Hyal (150 U mL^{-1}), and acetate buffer only. (B) Response of PMC-HA-MnO$_2$ to deactivated Hyal (150 U mL^{-1}) and Hyal triggered CA release from PMC-HA-MnO$_2$ after incubation in acetate buffer for 3 h.

activity. Fig. 5A shows the antibacterial effects of PMC-HA-MnO$_2$ concentration in the presence of 0.2 mmol L^{-1} H$_2$O$_2$ at pH 5.5. Obviously, PMC-HA-MnO$_2$ showed a concentration dependent bactericidal effect. Over 90% bacteria were killed in the presence of 300 μg mL^{-1} PMC-HA-MnO$_2$ due to the synergetic effect of "on-demand" CA release and CDT triggered by the bacterial microenvironment. Besides, 0.2 mmol L^{-1} H$_2$O$_2$ only had no bactericidal effect on all of the studied bacteria (Fig. S7). Fig. 5B gives the optical density (OD, 600 nm) of the bacteria incubated with six groups (PBS, PBS + H$_2$O$_2$, PLNPs@MSN-MnO$_2$, PLNPs@MSN-MnO$_2$ + H$_2$O$_2$, PMC-HA, PMC-HA-MnO$_2$ + H$_2$O$_2$) to illustrate the effect of combined antibacterial effect. The bacteria in PBS and PBS with H$_2$O$_2$ exhib-

ited negligible bacterial death. However, the bacteria survival rate obviously decreased in the presence of 300 μg mL^{-1} PLNPs@MSN-MnO$_2$ without CA loading due to the CDT effect of Mn^{2+}. PMC-HA (300 μg mL^{-1}) could kill over 70% of the bacteria because of CA release. The antibacterial activity of PMC-HA-MnO$_2$ (300 μg mL^{-1}) was further enhanced by combining CDT effect with CA release, leading to the survival rate of bacteria below 10%. The great antibacterial ability of PMC-HA-MnO$_2$ could also be attributed to its accurate targeting to the surface of bacteria and the in situ "on-demand" release of CA. Fig. 5D gives a visual representation of the above six groups. Unlike the excellent bactericidal performance in acidic environment, PMC-HA-MnO$_2$ had no bactericidal
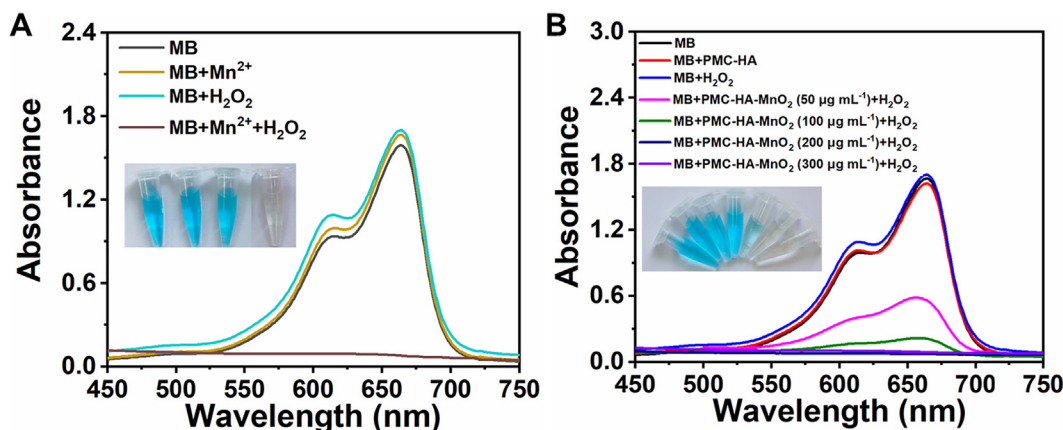
Fig. 4. (A) Effects of Mn^{2+} (0.5 mmol L^{-1}) or/and H_2O_2 (8 mmol L^{-1}) on the UV–vis absorption spectra (inset, the corresponding photo) of MB (10 mg L^{-1}) in 25 mmol L^{-1} $NaHCO_3$ aqueous solution. (B) MB degradation spectra and the photo (inset) with different concentrations of PMC-HA-MnO_2 ($NaHCO_3$, 25 mmol L^{-1}; H_2O_2, 8 mmol L^{-1}).
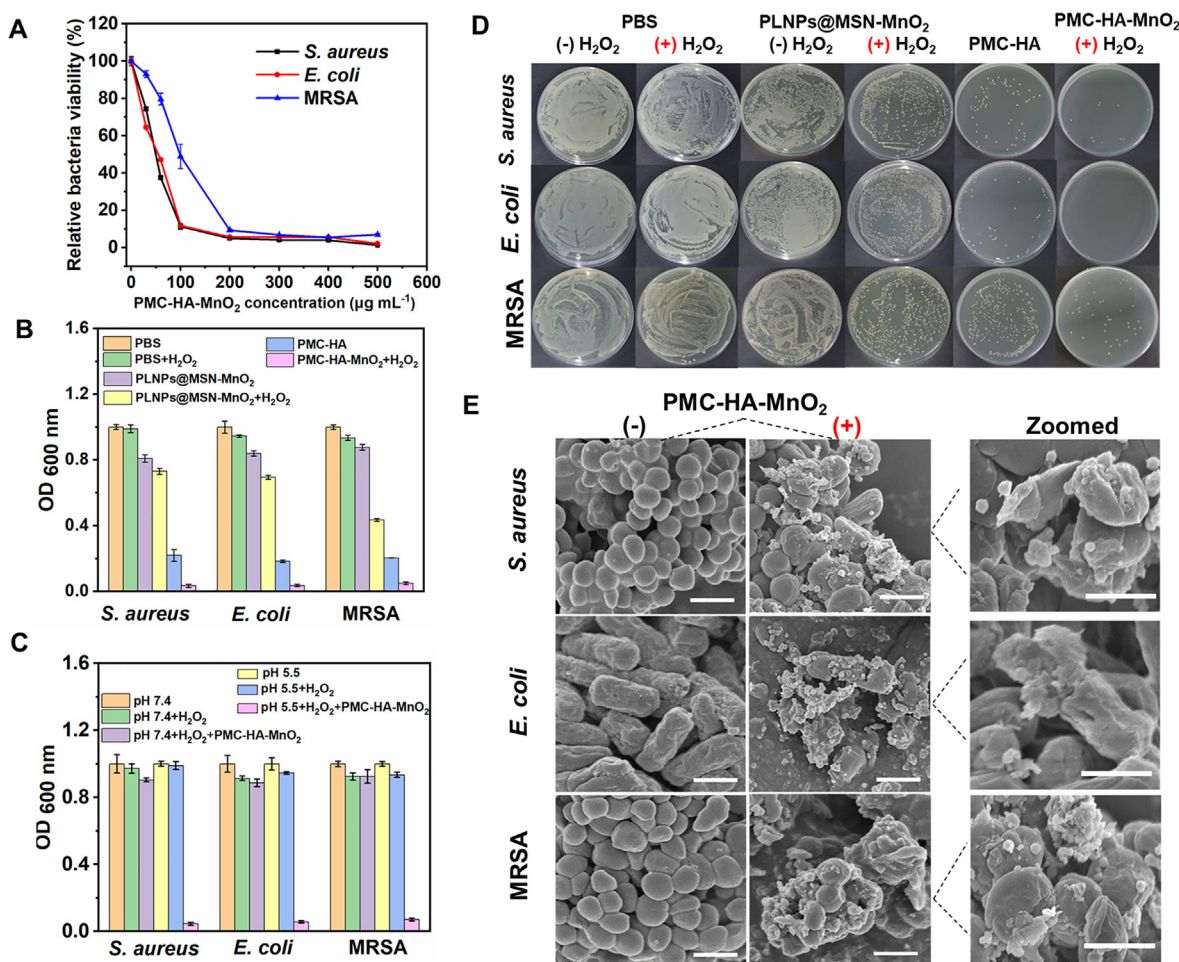

Fig. 5. (A) Effect of PMC-HA-MnO_2 concentration on the bacterial viabilities of *S. aureus*, *E. coli* and MRSA (pH 5.5, H_2O_2, 0.2 mmol L^{-1}). (B) $OD_{600\ nm}$ of bacteria suspension treated by different groups (pH 5.5, H_2O_2, 0.2 mmol L^{-1}). (C) $OD_{600\ nm}$ of bacteria suspension treated by PMC-HA-MnO_2 at pH 7.4 and pH 5.5 with H_2O_2 (0.2 mmol L^{-1}). (D) Photographs of bacterial colonies after exposure to different groups. (E) SEM images of *S. aureus*, *E. coli* and MRSA (-) and (+) treated by PMC-HA-MnO_2 (300 µg mL^{-1}) with H_2O_2 (0.2 mmol L^{-1}). Scale bar was 1 µm. Results are presented as mean ± SD (n ≥ 3).

effect in pH 7.4 with more than 90% bacteria survival (Fig. 5C), making PMC-HA-MnO_2 harmless to normal cells in physiological environment. Scanning electron microscope (SEM) images indicate that the three kinds of bacteria without treatment remained intact single cell structure, whereas PMC-HA-MnO_2 made the bacteria

merged and the cell structures collapse, implying the disruption of the bacteria by PMC-HA-MnO_2 (Fig. 5E).

The interaction between PMC-HA-MnO_2 and bacteria was observed intuitively on the laser confocal scanning microscopy (LCSM). After incubation with PMC-HA-MnO_2 for 20 min, *S. aureus*,

E. coli and MRSA cells dispalyed bright red luminescence, indicating the bacteria were successfully labeled (Fig. 6). The results show that PMC-HA-MnO$_2$ possessed the ability to attach to the surface of bacteria and light up the bacteria, which is of great importance for the therapy process monitoring and effective antibacterial treatment.

3.6. Toxicity test of PMC-HA-MnO$_2$

MTT assay was conducted to evaluate the cytotoxicity of PMC-HA-MnO$_2$. 3T3 and AGS cells gave over 85% viability at a high dose of 500 μg mL^{-1}, exhibiting low cytotoxicity of PMC-HA-MnO$_2$ (Fig. S8A and B). The *in vivo* toxicity of PMC-HA-MnO$_2$ was evaluated by histological studies of five major organs (heart, liver, spleen, lung and kidney) harvested from the sacrificed mice after 10-day treatment. The mice without any treatment were used as the control group. The organs in the mice injected with PMC-HA-MnO$_2$ showed no appreciable histological abnormalities or lesion at 10 days after injection (Fig. S8C). The body weights for all groups of mice exhibited similar increase during the 10 days. The PMC-HA-MnO$_2$ treated group did not show obvious weight loss or abnormal behavior, suggesting that PMC-HA-MnO$_2$ had no effect on the growth of mice (Fig. S9). The above results reveal that the PMC-HA-MnO$_2$ nanoplatform has good biocompatibility.

3.7. Turn-on PL imaging of bacterial infection in vivo

The excellent targeting ability and PL "turn-on" performance *in vitro* inspired us to investigate the performance of PMC-HA-MnO$_2$ for *in vivo* imaging in bacterial infection with MRSA infected mice. For comparison, the mice with subcutaneous abscess were divided into three groups and intravenously injected with PLNPs@MSN, PMC-HA and PMC-HA-MnO$_2$, respectively. The NIR afterglow images of mice were obtained at the designated time points after 2-min LED light illumination. Fig. 7A illustrates the treatment schedule of PMC-HA-MnO$_2$. No obvious PL signal was observed at the site of bacterial infection in the mice injected with PLNPs@MSN at all time points. In contrast, the mice injected with PMC-HA-MnO$_2$ showed restored PL signal at 4 h and the PL signal became more obvious from 6 h to 6 days in the abscess area, indicating that a certain amount of PMC-HA-MnO$_2$ was accumulated and triggered in the bacterial infection *in vivo*. However, as the inflammation gradually healed and the scab fell off after therapy, PL signal was reduced at days 8 and 10. To further demonstrate the sensitivity of PL "turn-on" imaging to the targeted locations, PMC-HA was also intravenously injected into the subcutaneous abscess mice for comparison. PMC-HA also possessed the ability to target the infection sites due to the modification of HA. However, the target position was unclear before 12 h because the "always-on" signal obscured the response signal at the focal site (Fig. S10). Therefore, the "turn-on" imaging is significance for practical clinical diagnosis due to the lower background and higher sensitivity than "always-on" imaging. The relative PL intensity of isolated organs showed most PMC-HA-MnO$_2$ in liver and spleen because of the phagocytosis of reticuloendothelial system, but very little in other organs (Fig. 7C and S11).

3.8. PMC-HA-MnO$_2$ for in vivo therapy

The MRSA-infected mice were randomly divided into three groups (control group treated with PBS only, two experimental groups treated with PMC-HA and PMC-HA-MnO$_2$, respectively) to evaluate PMC-HA-MnO$_2$ for *in vivo* therapy. The PMC-HA-MnO$_2$-treated group showed much faster skin abscess healing than the other groups at the same time points (Fig. 8A). The abscess of the mice in PMC-HA-MnO$_2$ group disappeared with the scars fell off
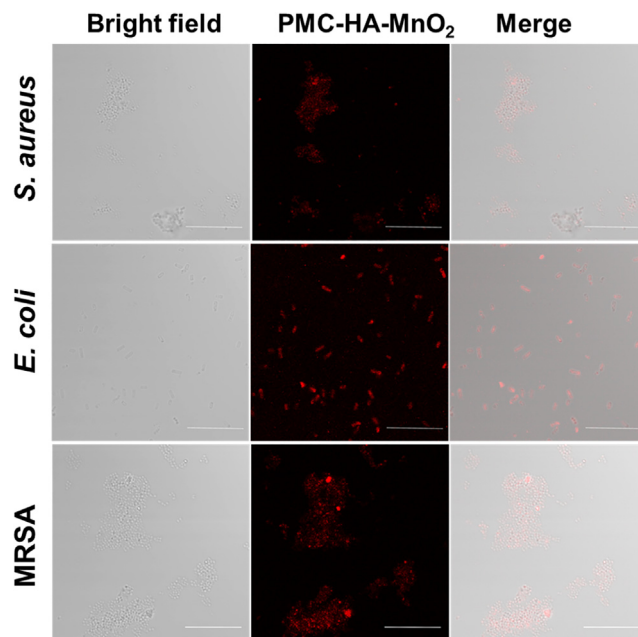

Fig. 6. Representative LCSM images of *S. aureus*, *E. coli* and MRSA incubated with PMC-HA-MnO$_2$ (PMC-HA-MnO$_2$, 300 μg mL^{-1}; pH 5.5, H$_2$O$_2$, 0.2 mmol L^{-1}). Scale bar is 10 μm.

after 10-day treatment, whereas the obvious scab of the mice in PMC-HA and PBS group still remained. (Fig. 8B) shows that the PMC-HA-MnO$_2$ treated group after 10-day treatment had reconstructed hair follicle tissue for antibacterial effect and exhibited a more uniform epithelial cell layer. Instead, PBS group displayed many aggregated inflammatory cells. The infected skin tissues were counted using the standard bacterial culture method after 10 days to verify the efficiency of infection treatment (Fig. 8C). The quantitative bacterial colonies remarkably decreased in the PMC-HA-MnO$_2$ treated mice, indicating the good recovery from infection. PMC-HA-MnO$_2$ group gave dramatically lower levels of serum IL-1β and IL-6 than PBS group, but similar levels to healthy mice (Fig. 8D and E), verifying the good therapeutic effect of the infected mice in PMC-HA-MnO$_2$ group.

4. Conclusion

In summary, we have reported a bacterial microenvironment triggered nanoplatform (PMC-HA-MnO$_2$) for PL "turn-on" imaging, "on-demand" CA release and the synergetic CDT for bacteria imaging and killing. Different from the fibrous dressings fixed CA inside [14], our design integrates "on-demand" CA delivery with synergistic effect of CDT, and greatly improves the antibacterial effect of CA. Moreover, the previous application of fibrous dressings is limited to the surface wound infections, whereas our integrated nanoplatform enables the application for the therapy of bacterial infections *in vivo*. Compared to previous "on-demand" delivery system[45], our PMC-HA-MnO$_2$ nanoplatform endows the nanocarrier with additional autofluorescence-free PL imaging ability, which is of significance in offering timely and effective antibacterial stewardship during the whole therapy. The antibacterial system has been successfully applied for healing MRSA-infected subcutaneous abscesses in mice without damage to normal tissues. In light of increasing risk of antibiotic resistance, the developed nanoplatform has great potential in visualized treatment of MDR bacterial infection with no microbial drug resistance.
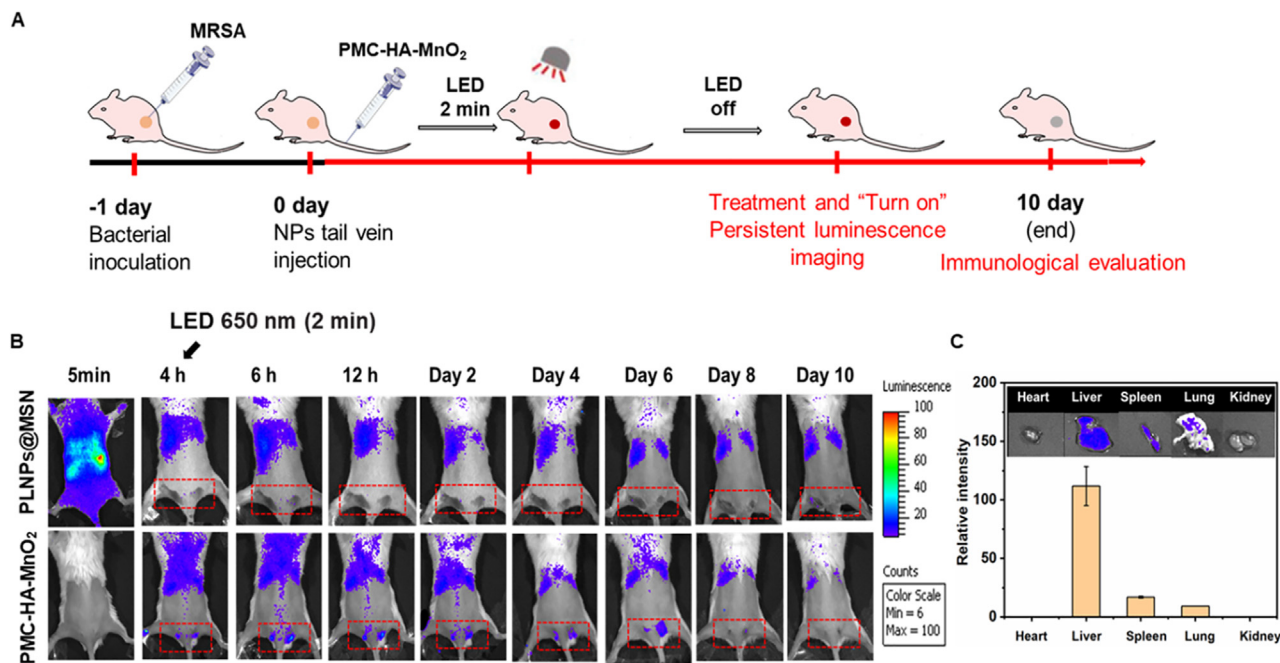
Fig. 7. (A) Treatment schedule of PMC-HA-MnO$_2$ for PL "turn-on" imaging and "on-demand" CA release combined with CDT for bacterial infections in mice. (B) *In vivo* PL "turn-on" imaging of MRSA-infected mice after injection of PLNPs@MSN or PMC-HA-MnO$_2$. (C) *In vivo* PL images and relative PL intensity of major organs for the mice 10 days after PMC-HA-MnO$_2$ injection. The liver PL intensity as control; error bar, one SD (n = 3).
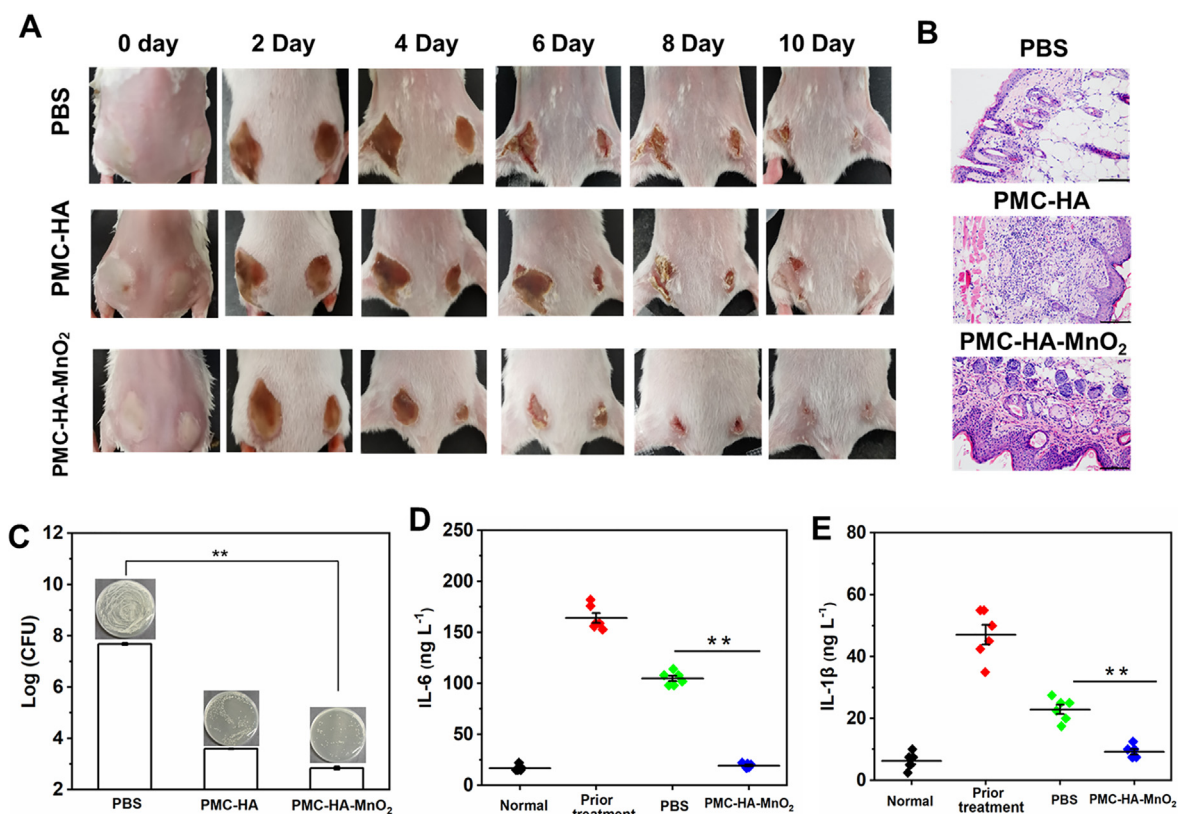

Fig. 8. (A) Photos of MRSA-infected site of mice after various treatments for 10 days. (B) H&E staining for histological examination of the skin tissue slices. (C) Photos and corresponding results of bacterial cultures for the tissues of MRSA-infected mice after 10-days treatment. (D) Serum IL-6 and (E) IL-1β level of MRSA-infected mice on day 10 after treatment. **Denotes significant difference (p < 0.001).

CRediT authorship contribution statement

Bei-Bei Wang: Conceptualization, Investigation, Methodology, Data curation, Writing – original draft. **Li-Xia Yan:** Conceptualization, Investigation, Methodology, Data curation, Writing – original draft. **Li-Jian Chen:** Methodology, Investigation. **Xu Zhao:** Methodology, Validation. **Xiu-Ping Yan:** Conceptualization, Supervision, Writing – review & editing, Funding acquisition.

Declaration of Competing Interest

The authors declare that they have no known competing financial interests or personal relationships that could have appeared to influence the work reported in this paper.

Acknowledgements

Appendix A. Supplementary material

Supplementary data to this article can be found online at https://doi.org/10.1016/j.jcis.2021.11.125.

References

[1] S.B. Levy, B. Marshall, Antibacterial resistance worldwide: causes, challenges and responses, Nat. Med. 10 (S12) (2004) S122–S129.

[2] E.D. Brown, G.D. Wright, Antibacterial drug discovery in the resistance era, Nature 529 (7586) (2016) 336–343.

[3] L. Wang, J. Yang, X. Yang, Q. Hou, S. Liu, W. Zheng, Y. Long, X. Jiang, Mercaptophenylboronic Acid-activated gold nanoparticles as nanoantibiotics against multidrug-resistant bacteria, ACS Appl. Mater. Interfaces 12 (46) (2020) 51148–51159.

[4] J. Meng, Z. Hu, M. He, J. Wang, X. Chen, Gold nanocluster surface ligand exchange: an oxidative stress amplifier for combating multidrug resistance bacterial infection, J. Colloid Interf. Sci. 602 (2021) 846–858.

[5] Z. Luo, H. Cui, J. Guo, J. Yao, X. Fang, F. Yan, B. Wang, H. Mao, Poly(ionic liquid)/Ce-based antimicrobial nanofibrous membrane for blocking drug-resistance dissemination from MRSA-infected wounds, Adv. Funct. Mater. 31 (2021) 2100336.

[6] W. Li, K. Dong, J. Ren, X. Qu, A β-lactamaseimprinted responsive hydrogel for the treatment of antibiotic-resistant bacteria, Angew. Chem. Int. Ed. 55 (28) (2016) 8049–8053.

[7] M.F. Chellat, L. Raguž, R. Riedl, Targeting antibiotic resistance, Angew. Chem. Int. Ed. 55 (23) (2016) 6600–6626.

[8] X. Sun, J. Sun, Y. Sun, C. Li, J. Fang, T. Zhang, Y. Wan, L. Xu, Y. Zhou, L. Wang, B. Dong, Oxygen self-sufficient nanoplatform for enhanced and selective antibacterial photodynamic therapy against anaerobe-induced periodontal disease, Adv. Funct. Mater. 31 (2021) 2101040.

[9] S.R. Norrby, C.E. Nord, R. Finch, Lack of development of new antimicrobial drugs: a potential serious threat to public health, Lancet Infect. Dis. 5 (2005) 115–119.

[10] D.N. Amato, D.V. Amato, O.V. Mavrodi, D.A. Braasch, S.E. Walley, J.R. Douglas, D.V. Mavrodi, D.L. Patton, Destruction of opportunistic pathogens via polymer nanoparticle-mediated release of plant-based antimicrobial payloads, Adv. Healthcare Mater. 5 (2016) 1094.

[11] T. Ran, S. Jacqueline, I. Ashraf, Antimicrobial activity of various essential oils and their application in active packaging of frozen vegetable products, Food Chem. 360 (2021) 129956.

[12] R.F. Landis, A. Gupta, Y.-W. Lee, L.-S. Wang, B. Golba, B. Couillaud, R. Ridolfo, R. Das, V.M. Rotello, Crosslinked polymer-stabilized nanocomposites for the treatment of bacterial biofilms, ACS Nano 11 (2017) 946.

[13] G.D. Wright, Opportunities for natural products in 21st century antibiotic discovery, Nat. Prod. Rep. 34 (7) (2017) 694–701.

[14] I. Liakos, L. Rizzello, H. Hajiali, V. Brunetti, R. Carzino, P.P. Pompa, A. Athanassiou, E. Mele, Fibrous wound dressings encapsulating essential oils as natural antimicrobial agents, J. Mater. Chem. B 3 (8) (2015) 1583–1589.

[15] K. Feng, P. Wen, H. Yang, N. Li, W.Y. Lou, M.H. Zong, H. Wu, Enhancement of the antimicrobial activity of cinnamon essential oil-loaded electrospun nanofilm by the incorporation of lysozyme, RSC Adv. 7 (3) (2017) 1572–1580.

[16] M. Ramasamy, J.-H. Lee, J. Lee, Development of gold nanoparticles coated with silica containing the antibiofilm drug cinnamaldehyde and their effects on pathogenic bacteria, Int. J. Nanomed. 12 (2017) 2813–2828.

[17] B. Ding, S. Shao, F. Jiang, P. Dang, C. Sun, S. Huang, P. Ma, D. Jin, A.A. Al Kheraif, J. Lin, MnO₂-disguised upconversion hybrid nanocomposite: an ideal architecture for tumor microenvironment-triggered UCL/MR bioimaging and enhanced chemodynamic therapy, Chem. Mater. 31 (2019) 2651–2660.

[18] T. He, C. Jiang, J. He, Y. Zhang, G. He, J. Wu, J. Lin, X. Zhou, P. Huang, Manganese-dioxide-coating-instructed plasmonic modulation of gold nanorods for activatable duplex-imaging-guided NIR-II photothermal-chemodynamic therapy, Adv. Mater. 33 (2021) 2008540.

[19] L.-H. Fu, Y.-R. Hu, C. Qi, T. He, S. Jiang, C. Jiang, J. He, J. Qu, J. Lin, P. Huang, Biodegradable manganese-doped calcium phosphate nanotheranostics for traceable cascade reaction-enhanced anti-tumor therapy, ACS Nano 13 (12) (2019) 13985–13994.

[20] T. He, X. Qin, C. Jiang, D. Jiang, S. Lei, J. Lin, W.-G. Zhu, J. Qu, P. Huang, Tumor pH-responsive metastable-phase manganese sulfide nanotheranostics for traceable hydrogen sulfide gas therapy primed chemodynamic therapy, Theranostics 10 (6) (2020) 2453–2462.

[21] X. Lin, S. Liu, X. Zhang, R. Zhu, S. Chen, X. Chen, J. Song, H. Yang, An ultrasound activated vesicle of Janus Au-MnO nanoparticles for promoted tumor penetration and sono-chemodynamic therapy of orthotopic liver cancer, Angew. Chem. Int. Ed. 59 (4) (2020) 1682–1688.

[22] J. Xiao, G. Zhang, R. Xu, H. Chen, H. Wang, G. Tian, B. Wang, C. Yang, G. Bai, Z. Zhang, H. Yang, K. Zhong, D. Zou, Z. Wu, A pH-responsive platform combining chemodynamic therapy with limotherapy for simultaneous bioimaging and synergistic cancer therapy, Biomaterials 216 (2019) 119254.

[23] L.-S. Lin, J. Song, L. Song, K. Ke, Y. Liu, Z. Zhou, Z. Shen, J. Li, Z. Yang, W. Tang, G. Niu, H.-H. Yang, X. Chen, Simultaneous Fenton-like ion delivery and glutathione depletion by MnO₂-based nanoagent to enhance chemodynamic therapy, Angew. Chem. Int. Ed. 57 (18) (2018) 4902–4906.

[24] L. Feng, R. Xie, C. Wang, S. Gai, F. He, D. Yang, P. Yang, J. Lin, Magnetic targeting, tumor microenvironment-responsive intelligent nanocatalysts for enhanced tumor ablation, ACS Nano 12 (11) (2018) 11000–11012.

[25] C. Lu, C. Zhang, P. Wang, Y. Zhao, Y. Yang, Y. Wang, H. Yuan, S. Qu, X. Zhang, G. Song, K. Pu, Light-free generation of singlet oxygen through manganese-thiophene nanosystems for pH-responsive chemiluminescence imaging and tumor therapy, Chem 6 (9) (2020) 2314–2334.

[26] X. Gao, Y. Cui, R.M. Levenson, L.W.K. Chung, S. Nie, *In vivo* cancer targeting and imaging with semiconductor quantum dots, Nat Biotechnol. 22 (8) (2004) 969–976.

[27] S.-H. Chiu, G. Gedda, W.M. Girma, J.-K. Chen, Y.-C. Ling, A.V. Ghule, K.-L. Ou, J.-Y. Chang, Rapid fabrication of carbon quantum dots as multifunctional nanovehicles for dual-modal targeted imaging and chemotherapy, Acta Biomater. 46 (2016) 151–164.

[28] L. Ming, L. Song, J. Xu, R. Wang, J. Shi, M. Chen, Y. Zhang, Smart manganese dioxide-based lanthanide nanoprobes for triple negative breast cancer precise gene synergistic chemodynamic therapy, ACS Appl. Mater. Interfaces 13 (30) (2021) 35444–35455.

[29] N. Kandoth, S. Barman, A. Chatterjee, S. Sarkar, A.K. Dey, S.K. Pramanik, A. Das, Photoactive lanthanide-based upconverting nanoclusters for antimicrobial applications, Adv. Funct. Mater. 31 (2021) 2104480.

[30] L.-J. Chen, X. Zhao, X.-P. Yan, Cell-penetrating peptide-functionalized persistent luminescence nanoparticles for tracking J774A.1 macrophages homing to inflamed tissues, ACS Appl. Mater. Interfaces 11 (22) (2019) 19894–19901.

[31] L.-X. Yan, L.-J. Chen, X. Zhao, X.-P. Yan, pH switchable nanoplatform for in vivo persistent luminescence imaging and precise photothermal therapy of bacterial infection, Adv. Funct. Mater. 30 (2020) 1909402.

[32] H.-J. Zhang, X. Zhao, L.-J. Chen, C.-X. Yang, X.-P. Yan, pH-driven targeting nanoprobe with dual-responsive drug release for persistent luminescence imaging and chemotherapy of tumor, Anal. Chem. 92 (1) (2020) 1179–1188.

[33] J. Visvalingam, K. Palaniappan, R.A. Holley, *In vitro* enhancement of antibiotic susceptibility of drug resistant *Escherichia coli* by cinnamaldehyde, Food Control 79 (2017) 288–291.

[34] J. Sun, Y. Fan, P. Zhang, X.u. Zhang, Q. Zhou, J. Zhao, L. Ren, Self-enriched mesoporous silica nanoparticle composite membrane with remarkable photodynamic antimicrobial performances, J. Colloid Interf. Sci. 559 (2020) 197–205.

[35] K.Y. Choi, H.S. Han, E.S. Lee, J.M. Shin, B.D. Almquist, D.S. Lee, J.H. Park, Hyaluronic acid-based activatable nanomaterials for stimuli responsive imaging and therapeutics: beyond CD44-mediated drug delivery, Adv. Mater. 31 (2019) 1803549.

[36] Y. Liu, A. Lin, J. Liu, X. Chen, X. Zhu, Y. Gong, G. Yuan, L. Chen, J. Liu, Enzyme-responsive mesoporous ruthenium for combined chemo-photothermal therapy of drug-resistant bacteria, ACS Appl. Mater. Interfaces 11 (30) (2019) 26590–26606.

[37] Q. Yuan, Y. Zhao, Z. Zhang, Y. Tang, On-demand antimicrobial agent release from functionalized conjugated oligomer-hyaluronic acid nanoparticles for

tackling antimicrobial resistance, ACS Appl. Mater. Interfaces 13 (1) (2021) 257–265.

[38] J. Wang, Q. Ma, X.-X. Hu, H. Liu, W. Zheng, X. Chen, Q. Yuan, W. Tan, Autofluorescence-free targeted tumor imaging based on luminous nanoparticles with composition-dependent size and persistent luminescence, ACS Nano 11 (8) (2017) 8010–8017.

[39] L.-J. Chen, X. Zhao, Y.-Y. Liu, X.-P. Yan, Macrophage membrane coated persistent luminescence nanoparticle@MOF-derived mesoporous carbon core–shell nanocomposites for autofluorescence-free imaging-guided chemotherapy, J. Mater. Chem. B 8 (35) (2020) 8071–8083.

[40] W. Zhu, Z. Dong, T. Fu, J. Liu, Q. Chen, Y. Li, R. Zhu, L. Xu, Z. Liu, Modulation of hypoxia in solid tumor microenvironment with MnO_2 nanoparticles to enhance photodynamic therapy, Adv. Funct. Mater. 26 (2016) 5490.

[41] M.-D. Liu, D.-K. Guo, R.-Y. Zeng, J.-J. Ye, S.-B. Wang, C.-X. Li, Y.-X. Sun, S.-X. Cheng, X.-Z. Zhang, Yolk-shell structured nanoflowers induced intracellular

oxidative/thermal stress damage for cancer treatment, Adv. Funct. Mater. 30 (2020) 2006098.

[42] P.A. Hyslop, D.B. Hinshaw, I.U. Scraufstatter, C.G. Cochrane, S. Kunz, K. Vosbeck, Hydrogen peroxide as a potent bacteriostatic antibiotic: implications for host defense, Free Radicals, Biol. Med. 19 (1) (1995) 31–37.

[43] C. Wang, Y. Xiao, W. Zhu, J. Chu, J. Xu, H. Zhao, F. Shen, R. Peng, Z. Liu, Photosensitizer-modified MnO_2 nanoparticles to enhance photodynamic treatment of abscesses and boost immune protection for treated mice, Small 16 (2020) 2000589.

[44] R. Deng, X. Xie, M. Vendrell, Y.-T. Chang, X. Liu, Intracellular glutathione detection using MnO_2-nanosheet-modified upconversion nanoparticles, J. Am. Chem. Soc. 133 (50) (2011) 20168–20171.

[45] P. Sun, Y. Zhang, X. Ran, C. Liu, Z. Wang, J. Ren, X. Qu, Phytochemical-encapsulated nanoplatform for "on demand" synergistic treatment of multidrug-resistant bacteria, Nano Res. 11 (7) (2018) 3762–3770.